Communications in Computational Chemistry
Commun. Comput. Chem., Vol. 1, No. 1, 81–87
doi: 10.4208/cicc.2025.84.02
Regular Article

Enhancing Optoelectronic Properties of Quasi-2D Ruddlesden–Popper Perovskites via Pseudo–Halogen Doping: A First–Principles Study on $Cs_2Pb(SCN)_2Br_2$

Peng Xiong[1,2,3,†], Jia-Ming Li[1,2,†], Zhi-Mi Zhang[3], Zhong-Yuan Wang[3], Jian Wu[1,2,*] and Chuan-Jia Tong[3,*]

[1] *International Institute for Materials Innovation, Nanchang University, Nanchang, 330031, China;*

[2] *School of Physics and Materials Science, Nanchang University, Nanchang, 330031, China;*

[3] *Institute of Quantum Physics, Hunan Key Laboratory of Nanophotonics and Devices, Hunan Key Laboratory of Super-Microstructure and Ultrafast Process, School of Physics, Central South University, Changsha 410083, China.*

[*] Corresponding authors: wujian@ncu.edu.cn (J. Wu), chuanjia.tong@csu.edu.cn (C.-J. Tong).

Received on 15 March 2025; Accepted on 11 April 2025

[†]: Peng Xiong and Jia-Ming Li contributed equally to this work.

Abstract

Two-dimensional (2D) Ruddlesden–Popper (RP) perovskites have been intensively investigated due to their superior stability and outstanding optoelectronic properties. Although A-site doping in quasi–2D RP–phase perovskites has been extensively studied, the effect of X–site doping remains unknown. Using first–principles calculations, this work demonstrates that SCN^- substitution in $Cs_2Pb(SCN)_2Br_2$ induces a structural transformation from isotropic to anisotropic through octahedral tilting along the b-axis, reducing octahedral spacing from 5.17 to 4.88 Å. This structural modification enhances carrier mobility, dramatically increases exciton binding energy from 30.47 to 145.39 meV, and improves defect tolerance compared to pristine Cs_2PbBr_4. These modifications synergistically suppress non-radiative recombination pathways while promoting radiative processes, so that improve its performance as a promising light–emitting diode (LED) material. These findings establish pseudo–halogen substitution as a promising strategy for optimizing carrier transport and radiative efficiency in low-dimensional perovskite LED devices.

Key words: Ruddlesden–Popper (RP) perovskites, LED, exciton binding energy, carrier mobility.

All–inorganic three–dimensional perovskites ABX_3 exhibit remarkable optoelectronic properties [1-8], achieving external quantum efficiencies (EQE) up to 32% in perovskite light–emitting diodes (PeLEDs) applications [9]. However, fundamental limitations arise from their inherently weak exciton binding energy (E_b) and structural instability [10-12]. The slow radiative (bimolecular) recombination rate in three–dimensional perovskites frequently results in free carriers (FCs) being captured by defects, leading to non–radiative recombination instead of radiative decay [13]. Two–dimensional (2D) and quasi–2D perovskites effectively address these limitations through quantum confinement effects, which enhance E$_b$ and improve structural stability through reduced dimensionality [14-16]. A critical factor governing the light–emitting diode (LED) performance of quasi–2D perovskites is the competition between radiative and non–radiative recombination channels, which is intrinsically linked to carrier mobility, E$_b$, and defect formation energy.

Layered lead halide perovskites have recently garnered attention due to their tunable optoelectronic properties and improved stability [16-18]. For example, $Cs_2Pb(SCN)_2Br_2$, a pseudo–halogen–doped 2D Ruddlesden–Popper (RP) perovskite, exhibits enhanced stability and quantum confinement effects [19-21]. Recent experimental investigations have established the fundamental properties and applications of the materials: Liao *et al.* successfully synthesized single crystal $Cs_2Pb(SCN)_2Br_2$ by the antisolvent vapor–assisted crystallization (AVC) method [22]. While Liu *et al.* prepared quasi–2D RP–phase perovskite $Cs_2Pb(SCN)_2Br_2$ polycrystalline wafer, and investigated its potential in X–ray detection [23]. Despite the promising photovoltaic properties demonstrated by this material, the fundamental mechanisms underlying their performance remain incompletely understood, especially the influence of pseudo–halogen doping in $Cs_2Pb(SCN)_2Br_2$. Specifically, the impact of such doping on radiative and non-radiative recombination processes requires further elucidation. Therefore, further theoretical research is needed to understand the microscopic mechanisms by which pseudo–halogen doping affects perovskite performance.

In this work, the $Cs_2Pb(SCN)_2Br_2$ and Cs_2PbBr_4 systems are presented as a comparative analysis to elucidate the influence of pseudo–halogen doping on their optoelectronic properties. Through first–principles calculations, we investigate the electronic structure, E$_b$, carrier mobility, and defect formation energetics. Our results indicate that SCN^- modifies the crystal structure, improves the structure stability, suppresses non–radiative pathways, and enhances carrier mobility. These improvements are attributed to reduced defect formation energies and optimized E$_b$, which collectively enhance radiative efficiency. The results establish pseudo–halogen engineering as a viable strategy for enhancing perovskite optoelectronic properties, offering a framework for designing high–performance LEDs.

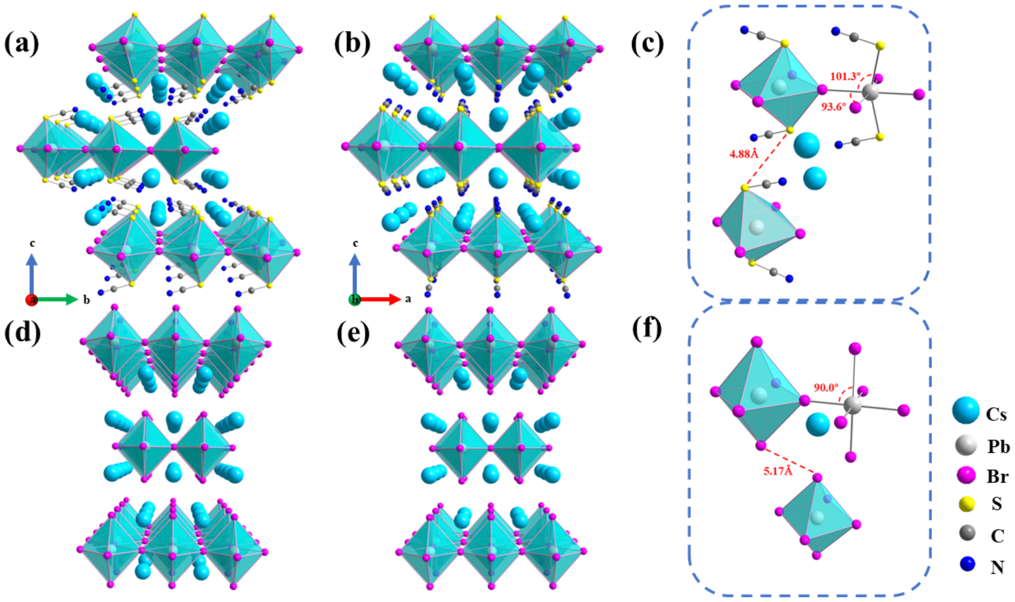

Figure 1. (a) Front view and (b) side view of the $Cs_2Pb(SCN)_2Br_2$. (c) Schematic of the octahedral distortion angle and octahedral spacing of the $Cs_2Pb(SCN)_2Br_2$. (d) Front and (e) side view of the Cs_2PbBr_4. (f) The schematic of the octahedral distortion angle and octahedral spacing of the Cs_2PbBr_4. The blue spheres represent Cs atoms, the white spheres represent Pb atoms, the purple spheres represent Br atoms, the yellow spheres represent S atoms, the grey spheres represent C atoms and the dark blue spheres represent N atoms.

The electronic structure and electronic properties were obtained using density functional theory (DFT) as implemented in the Vienna *ab initio* simulation package (VASP) [24-27]. The exchange–correlation energy was modeled using the generalized gradient approximation (GGA) with the Perdew–Burke–Ernzerhof (PBE) functional[28-30]. To accurately account for van der Waals (vdW) interactions, the Grimme DFT-D3 method with Becke–Johnson damping was employed [31-33]. All calculations were performed on a $2 \times 2 \times 2$ supercell, with a plane–wave cutoff energy of 500 eV. The optimization was carried out using a $2 \times 2 \times 1$ *k*–point mesh until the energy converged to 10^{-5} eV. Additionally, all atomic positions were relaxed until the maximum residual force on each atom was reduced to less than 0.01 eV/Å.

According to the deformation potential (DP) theory introduced by Bardeen and Shockley [34-35], the carrier mobility in crystalline materials is expressed by the following equation:

$$\mu_\beta^{3D} = \frac{e\langle\tau_\beta\rangle}{m^*} = \frac{2\sqrt{2\pi}eC_\beta^{3D}\hbar^4}{3(\kappa_B T)^{3/2}E_\beta^{3D}m^{*5/2}} \qquad (1)$$

where e is the electron charge, $\hbar$ is the approximate Planck constant, k_B is the Boltzmann constant, and T is the room temperature ($T = 300$ K). m^* is the effective mass. C_β^{3D} denotes the elastic modulus of the crystal along the transport direction, and E_β^{3D} denotes the deformation potential constant along the transport direction for holes at the valence band maximum (VBM) or for electrons at the conduction band minimum (CBM).

In this study, the Delta–Self–Consistent Field (ΔSCF) method [36-38] was employed to calculate the E_b. An electron is excited from the VBM to the CBM, and then the orbital positions are fixed during the calculation. To prevent unphysical occupation of the band edge states, only a single gamma point was used. The E_b was calculated as follows:

$$E_b = E_{(GS)} + E_g - E_{FE} \qquad (2)$$

where E_g is the band gap energy, $E_{(GS)}$ is the total ground state energy and E_{FE} is the total energy of the system with GS geometry and one FE (an electron was moved from the VBM to CBM).

The formation enthalpies $\Delta H_f\ (\alpha, q)$ of a complex defect in the supercell model，can be expressed as [39,40]:

$$\Delta H_f\ (\alpha, q) = E\ (\alpha, q) - E\ (\text{host}) + \sum n_i\ (E_i + \mu_i) \qquad (3)$$

Where E (α, q) and E (host) are the total energies of the supercell with and without defects, respectively. n_i is the number of i atoms added ($n_i < 0$) or removed ($n_i > 0$). In this equation, μ_i is the atomic chemical potential of constituent i referenced to the total energy E_i of its pure elemental solid or molecule.

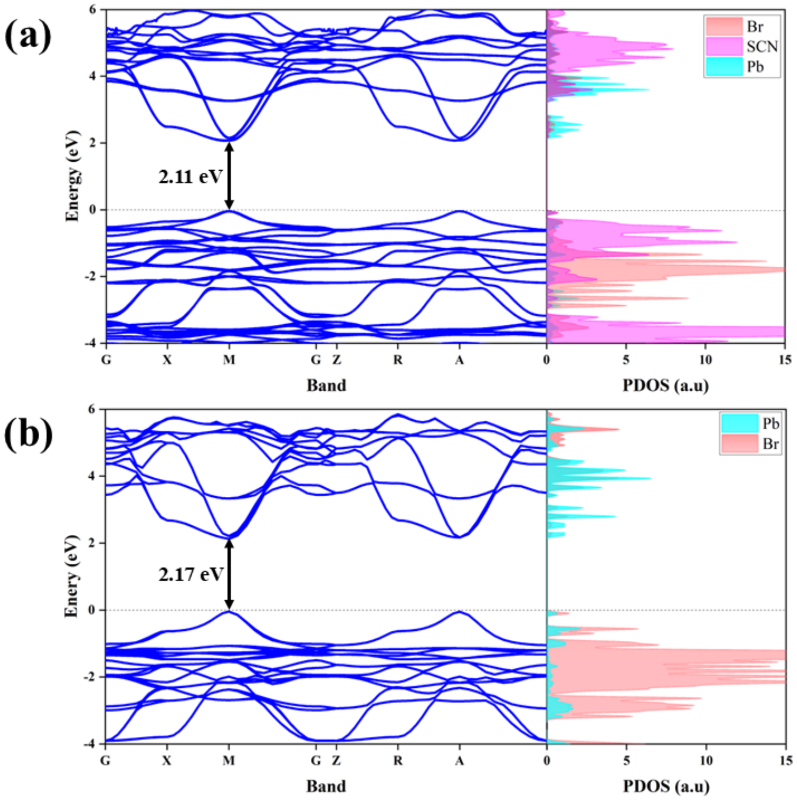

Figure 2. (a) Band structure and projected density of states of $Cs_2Pb(SCN)_2Br_2$ and (b) band structure and projected density of states of Cs_2PbBr_4.

The structures of quasi–2D RP–phase perovskites $Cs_2Pb(SCN)_2Br_2$ and Cs_2PbBr_4 are shown in Figure 1. Structural parameters are summarized in Table 1, revealing orthorhombic symmetry with closely matched lattice parameters. In $Cs_2Pb(SCN)_2Br_2$, the asymmetric electronic structure and geometry of SCN^- anions induce a layered $[Pb(SCN)_2Br_4]$ framework, where four Br^- anions occupy an octahedral plane as the shared corner, while two S–bonded SCN^- anions occupy the axial direction capping the octahedra. This chemical substitution significantly modifies the crystal structure: the SCN^- doping leads to octahedral tilting along the y axis, manifesting as pronounced in–plane anisotropy (Figure 1a&c). In contrast, Cs_2PbBr_4 exhibits a conventional quasi–2D RP–phase perovskite structure with aligned inorganic layers, resulting in in–plane isotropy. In addition, the axially–positioned SCN^- anions result in electronic and geometric asymmetry that stabilizes the 2D framework more effectively than spherical Br^- anions. Specifically, this doping distorted the original octahedral structure, casuing the maximum X–Pb–X bond angle deviating from 90° to 101.3°, while reducing the distance between the octahedra from 5.17 to 4.88 Å. The tilted octahedra and reduced interlayer distance together reduce the Coulombic distance between the well and the barrier, thereby enhancing the dielectric constant and improving charge transport.

Table 1. Lattice constants of $Cs_2Pb(SCN)_2Br_2$ and Cs_2PbBr_4.

	a (Å)	b (Å)	c (Å)	α	β	γ
$Cs_2Pb(SCN)_2Br_2$	5.99	6.06	17.86	90°	90°	90°
Cs_2PbBr_4	5.90	5.90	18.09	90°	90°	90°

In order to investigate the effect of structure changes on the electronic properties, the band structures of $Cs_2Pb(SCN)_2Br_2$ and Cs_2PbBr_4 are calculated, as shown in Figure 2a&b. The results indicate that doping with SCN^- leads to a modest band gap reduction from 2.17 to 2.11 eV ($\Delta = 0.06$ eV), while maintaining a direct band gap at the M point. Notably, no deep–level defect states are observed in the band gap region, indicating that SCN^- substitution preserves the fundamental electronic structure of the host material. The projected density of states (PDOS) analysis of the two structures, shown in Figure 2a&b, reveals the orbital electronic structure of both compounds. In Cs_2PbBr_4, the VBM primarily originates from Br–4*p* states with contributions from Pb–6*p* states, while the CBM is dominated by Pb–6*p* states with minor Br–4*p* orbital hybridization. Upon SCN^- doping, significant electronic states are introduced in the energy range of -1.5 to 0 eV, modifying the VBM character. The presence of SCN^- states near the VBM results in band edge modification, attributed to the hybridization between the SCN^- molecular orbitals and the host lattice states (Pb–6*p* and Br–4*p*).

Specifically, the nitrogen and sulfur atomic orbitals of the SCN$^-$ ligand introduce localized states that alter the electronic structure through orbital interactions, leading to the observed VBM shift and subsequent band gap reduction.

The reduced band gap facilitates better charge carrier dynamics by enhancing the overlap of electronic states, which could improve excitonic properties and radiative recombination efficiency. While the change in band gap magnitude is minimal, the redistribution of electronic density and the subsequent effects on optical and charge transport properties could have significant implications for the design and optimization of perovskite–based optoelectronic devices.

The minimal band gap variation (from 2.17 to 2.11 eV) upon SCN$^-$ doping maintains the suitability of the material for PLED applications, necessitating a detailed investigation of its optoelectronic properties in both pristine and doped systems. In order to facilitate more accurate calculations and a deeper understanding of the E_b, a schematic diagram illustrating exciton luminescence is also presented in Figure 3a. The diagram shows the energy–lattice deformation relationships for the ground state (GS), free carrier state (FC), free exciton state (FE), and exciton compound states (EC). In the process of exciton formation, electrons are excited from the GS to the FC state, becoming free carriers. These free carriers subsequently interact via Coulombic forces to form bound electron–hole pairs in the FE state. Radiative recombination in this state results in photon emission, which is a desirable process for LEDs. However, the presence of defects within the material can complicate this pathway. If defects act as trapping centers, excitons may become localized in the EC state, leading to either radiative recombination with altered efficiency or non–radiative recombination, which diminishes luminescence performance.

The calculated E_b is illustrated in Figure 3b. Upon SCN$^-$ doping, $Cs_2Pb(SCN)_2Br_2$ exhibits a substantial increase in E_b compared to Cs_2PbBr_4, from 30.47 to 145.39 meV. This significant enhancement of E_b, which quantifies the Coulomb interaction strength between the electrons and the holes, promotes the formation and stability of exciton pairs, providing $Cs_2Pb(SCN)_2Br_2$ particularly suitable for LED applications. The change in E_b is primarily attributed to the effective mass, as the band gap of the two materials does not undergo significant variation, as previously noted. From Table 2, it is evident that the electron effective masses in $Cs_2Pb(SCN)_2Br_2$ and Cs_2PbBr_4 are similar. However, the effective mass of the holes has increased by 56%, an increase in the effective mass of the exciton results in an increase in the kinetic energy, which hinders the separation of electrons and holes, thereby contributing to the increase in E_b.

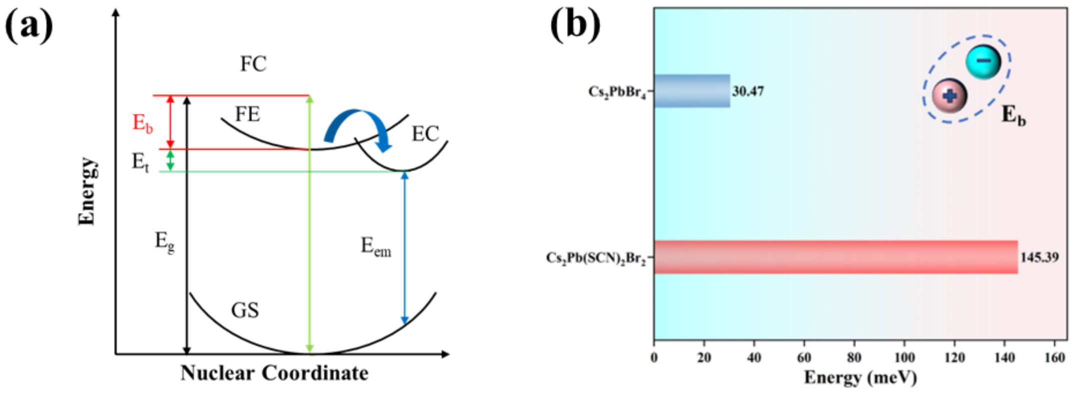

Figure 3. (a) Schematic diagram of free carriers (FC), free excitons (FE), and exciton complexes (EC) in $Cs_2Pb(SCN)_2Br_2$ and Cs_2PbBr_4 perovskite with GS indicating the ground state position, and E_b is the exciton binding energy. (b) The exciton binding energy of the $Cs_2Pb(SCN)_2Br_2$ and Cs_2PbBr_4.

Table 2. Effective Masses for Cs_2PbBr_4 and $Cs_2Pb(SCN)_2Br_2$.

system	carrier	m_x^*/m_0	m_y^*/m_0	$m_\parallel^*/m_0$
Cs_2PbBr_4	electron	0.21	0.21	0.21
	hole	0.25	0.25	0.25
$Cs_2Pb(SCN)_2Br_2$	electron	0.22	0.21	0.22
	hole	0.33	0.45	0.39

In LEDs, high carrier mobility plays a critical role in enhancing the efficiency of carrier recombination, which is directly tied to radiative luminescence efficiency. To quantify this effect, the carrier mobility in all–inorganic perovskite materials is calculated via deformation potential theory, as shown in Figure 4a. The results indicate that SCN$^-$ doping leads to an overall increase in carrier mobility, except for a slight decrease in hole mobility along the *x*–direction. This reduction is likely due to a significant increase in the effective mass of holes, as shown in Table 2, which is induced by the structural distortions caused by SCN$^-$ doping. Analysis of in–plane effective masses reveals $m_e^* \approx 0.21$ (electrons) remains constant, while m_h^* increases substantially from 0.25 to 0.33–0.45, the effective mass of holes exhibits a marked increase along specific directions. This increase in effective mass hinders exciton migration and reduces hole mobility, which partially offsets the overall mobility enhancement provided by SCN$^-$ doping.

The doping of SCN$^-$ additionally modifies the mechanical properties of the material, particularly its Young's modulus. SCN$^-$ doping transforms the initially isotropic Cs_2PbBr_4 into an anisotropic system, primarily due to the formation of chain–like SCN$^-$ structures along the *y*–direction, which significantly increases the elastic modulus in this direction. Calculations of the Young's modulus for $Cs_2Pb(SCN)_2Br_2$, shown in Figure 4b, confirm this anisotropic behavior, revealing substantially higher modulus values along the *y*–direction compared to the *x*–direction. This directional dependence of elastic properties significantly influences carrier transport characteristics. The increased stiffness along the *y*–direction facilitates improved in–plane carrier transport, contributing to the overall improvement in carrier mobility. Despite the slight reduction in hole mobility along the *x*–direction, the net effect of SCN$^-$ doping is a significant increase in in–plane carrier mobility, particularly for electrons. Such anisotropy–driven mobility enhancement is advantageous for applications where efficient charge transport and reduced carrier recombination losses are critical, such as in high–performance LEDs.

Pseudo-halogen atoms, such as SCN^-, have a profound impact on the electronic characteristics and defect–related properties of materials [41]. In perovskite systems, defects play a critical role in determining the optoelectronic properties and long–term stability of the material. To better understand the effects of SCN^- doping, the defect formation energies for various intrinsic defects are calculated in both pristine and SCN^- doped structures. Figure 4c presents a schematic representation of common defects, including vacancy defects, anti–site defects, and interstitial defects, while their corresponding defect formation energies are illustrated in Figure 4d. Among the calculated defects, the vacancy defect of lead (V_{Pb}) exhibits the lowest formation energy, with values of -1.11 eV and -0.45 eV in the undoped and SCN^- doped structures, respectively. The negative formation energies indicate that V_{Pb} defects are thermodynamically favorable under standard conditions. However, upon SCN^- doping, the defect formation energy for V_{Pb} increases significantly, suggesting that SCN^- incorporation suppresses the formation of this defect. This suppression is particularly critical, as V_{Pb} defects are known to facilitate non–radiative recombination, thereby adversely affecting luminescence efficiency. Beyond V_{Pb}, the formation energies of other intrinsic defects, such as anti-site and interstitial defects, also exhibit an upward trend with SCN^- doping. The overall increase in defect formation energies indicates that the introduction of SCN^- strengthens the stability and defect tolerance. The reduction in the likelihood of defect formation has significant implications for the optoelectronic properties of the materials. Reduced defect density enhances radiative recombination efficiency, directly beneficial for improving the luminescence performance of LEDs. These findings demonstrate that SCN^- doping synergistically improves defect tolerance and optoelectronic performance, making these materials particularly suitable for advanced applications in LED devices.

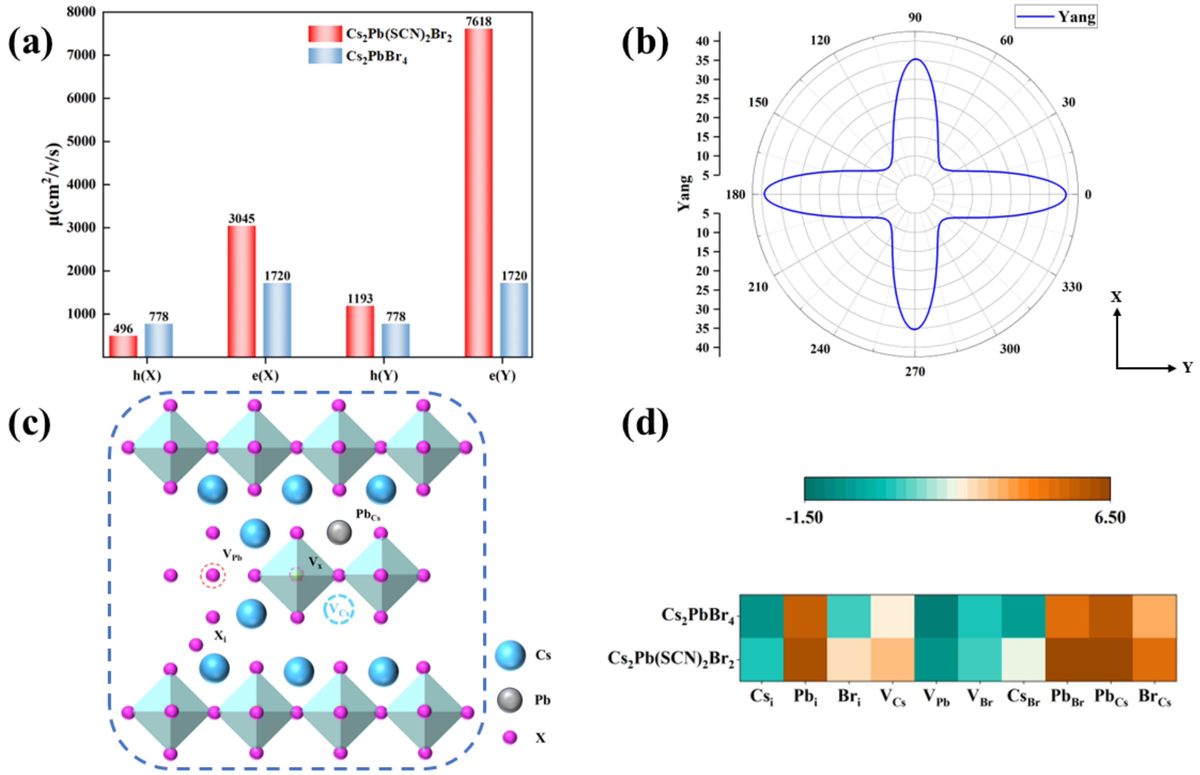

Figure 4. (a) Mobility of electrons and holes in the *x* and *y* directions in the plane. (b) Young's modulus plot of the $Cs_2Pb(SCN)_2Br_2$. (c) Schematic diagram of popular intrinsic defects in $Cs_2Pb(SCN)_2Br_2$ and Cs_2PbBr_4. (d) Image of defect formation energy magnitudes for some of the defects in different systems.

In summary, we have performed systematic calculations on the luminescence properties of SCN^- doped crystal structures in quasi–2D RP–phase perovskites. The E_b, carrier mobility, and defect formation energy are calculated for the radiative and non-radiative recombination. Additionally, the impact of pseudo–halogen atoms on the luminescence properties of the all–inorganic perovskite material and the underlying mechanism are investigated. The results show that when SCN^- is doped, the stability of the structure, the transport properties as well as the photovoltaic properties can be effectively improved, which can be applied into both experimental and practical applications. These insights not only deepen our understanding of the structure–property relationships in SCN^- doped perovskites but also provide valuable guidance for the rational design and optimization of advanced luminescent and photovoltaic materials. The exceptional performance of SCN^- doped perovskite highlights its potential for both experimental exploration and practical applications in next–generation optoelectronic devices.

Acknowledgements

This work was financially supported by the National Natural Science Foundation of China (No. 12474180) and Natural Science

Foundation of Hunan Province (Grant No. 2024JJ6481). We are grateful for resources from the High-Performance Computing Center of Central South University. We also acknowledge resources from the Hefei Advanced Computing Center.

References

[1] Sun Y., Ge L., Dai L. Bright and stable perovskite light-emitting diodes in the near-infrared range. *Nature*, **615** (2023), 830-835.

[2] Hassan Y., Park J.H., Crawford M.L. Ligand-engineered bandgap stability in mixed-halide perovskite LEDs. *Nature*, **591** (2021), 72-77.

[3] Wang Z.Y., Ye H.Q., Wang K.F. Superior photovoltaic performance of BF4-doped perovskite rationalized by *ab initio* nonadiabatic molecular dynamics. *Appl. Phys. Lett.*, **123** (2023).

[4] Shen X., Zhang X., Wang Z. Bright and efficient pure red perovskite nanocrystals light-emitting devices via *in situ* modification. *Adv. Funct. Mater.*, **32** (2022), 2110048.

[5] Lee J.-W., Tan S., Seok S.I. Rethinking the A cation in halide perovskites. *Science*, **375** (2022), eabj1186.

[6] Chu W., Saidi W.A., Zhao J. Soft lattice and defect covalency rationalize tolerance of β-CsPbI3 perovskite solar cells to native defects. *Angew. Chem. Int. Ed.*, **59** (2020), 6435-6441.

[7] Dong Q., Fang Y., Shao Y. Electron-hole diffusion lengths > 175 μm in solution-grown CH3NH3PbI3 single crystals. *Science*, **347** (2015), 967-970.

[8] Zhao J., Zhao L., Deng Y. Perovskite-filled membranes for flexible and large-area direct-conversion X-ray detector arrays. *Nat. Photonics*, **14** (2020), 612-617.

[9] Li M., Yang Y., Kuang Z. Acceleration of radiative recombination for efficient perovskite LEDs. *Nature*, **630** (2024), 631-635.

[10] Zhang P., Hua Y., Xu Y. Ultrasensitive and robust 120 keV hard X-ray imaging detector based on mixed-halide perovskite CsPbBr3-I single crystals. *Adv. Mater.*, **34** (2022), 2106562.

[11] Zhu W., Wang S., Zhang X. Ion migration in organic–inorganic hybrid perovskite solar cells: current understanding and perspectives. *Small*, **18** (2022), 2105783.

[12] Zhang M., Zhao W., Xin D. Solvent-free laminated fabrication of lead halide perovskites for sensitive and stable X-ray detection. *J. Phys. Chem. Lett.*, **12** (2021), 6961-6966.

[13] Cheng L., Jiang T., Cao Y. Multiple-quantum-well perovskites for high-performance light-emitting diodes. *Adv. Mater.*, **32** (2020), 1904163.

[14] Shen Y., Liu Y., Ye H. Centimeter-sized single crystal of two-dimensional halide perovskites incorporating straight-chain symmetric diammonium ion for X-ray detection. *Angew. Chem. Int. Ed.*, **59** (2020), 14896-14902.

[15] He X., Xia M., Wu H. Quasi-2D perovskite thick film for X-ray detection with low detection limit. *Adv. Funct. Mater.*, **32** (2022), 2109458.

[16] Li M., Li H., Li W. Oriented 2D perovskite wafers for anisotropic X-ray detection through a fast tableting strategy. *Adv. Mater.*, **34** (2022), 2108020.

[17] Zhang F., Kim D.H., Lu H. Enhanced charge transport in 2D perovskites via fluorination of organic cation. *J. Am. Chem. Soc.*, **141** (2019), 5972-5979.

[18] Blancon J.C., Stier A.V., Tsai H. Scaling law for excitons in 2D perovskite quantum wells. *Nat. Commun.*, **9** (2018), 2254.

[19] Xing X., Li J., Breen J.P. Structural dynamics of a novel pseudohalide perovskite Cs2Pb(SeCN)2Br2 investigated with nonlinear infrared spectroscopy. *J. Phys. Chem. C*, **127** (2023), 14283-14292.

[20] Guo S., Mao Y., Chen C. Pressure distinguishes the dual emissions in pseudohalide 2D Ruddlesden–Popper perovskite Cs2Pb(SCN)2Br2. *CCS Chemistry*, **6** (2024), 1748-1756.

[21] Liao M.Y., Chiang Y.C., Chen C.H. Two-dimensional Cs2Pb(SCN)2Br2-based photomemory devices showing a photoinduced recovery behavior and an unusual fully optically driven memory behavior. *ACS Appl. Mater. Interfaces*, **12** (2020), 36398-36408.

[22] Liao C.H., Chen C.H., Bing J. Inorganic-cation pseudohalide 2D Cs2Pb(SCN)2Br2 perovskite single crystal. *Adv. Mater.*, **34** (2022), 2104782.

[23] Liu D., Di H., Ren J. X-site substituted 2D Cs2Pb(SCN)2Br2 perovskites for X-ray detection. *Small*, **19** (2023), 2304201.

[24] Kresse G., Furthmüller J. Efficient iterative schemes for *ab initio* total-energy calculations using a plane-wave basis set. *Phys. Rev. B*, **54** (1996), 11169-11186.

[25] Kresse G., Furthmüller J. Efficiency of *ab initio* total-energy calculations for metals and semiconductors using a plane-wave basis set. *Comput. Mater. Sci.*, **6** (1996), 15-50.

[26] Wang K.P., Wu Z.W., Wang K.F. Detrimental defect cooperativity at TiO2/CH3NH3PbI3 interface: decreased stability, enhanced ion diffusion, and reduced charge lifetime and transport. *ACS Energy Lett.*, **9** (2024), 5888-5897.

[27] Wang Z.Y., Wang K.F., Jin J.J. Enhanced thermodynamic stability and carrier lifetime in BF4-doped wide-band-gap perovskite solar cells. *Phys. Rev. B*, **110** (2024), 045142.

[28] Perdew J.P., Burke K., Ernzerhof M. Generalized gradient approximation made simple. *Phys. Rev. Lett.*, **77** (1996), 3865-3868.

[29] Zhu A.Y., Ding R.X., Xu H.T. Cu-Zn cation disorder in kesterite Cu2ZnSn(SxSe1–x)4 solar cells. *ACS Energy Lett.*, **9** (2024), 497-503.

[30] Hao N.J., Ding R.X., Tong C.J. Heterogeneity of grain boundary properties in Cu2ZnSnS4: a first-principles study. *J. Appl. Phys.*, **133** (2023).

[31] Grimme S., Ehrlich S., Goerigk L. Effect of the damping function in dispersion-corrected density functional theory. *J. Comput. Chem.*, **32** (2011), 1456-1465.

[32] Tong C.J., Cai X., Zhu A.Y. How hole injection accelerates both ion migration and nonradiative recombination in metal halide perovskites. *J. Am. Chem. Soc.*, **144** (2022), 6604-6612.

[33] Grimme S., Antony J., Ehrlich S. A consistent and accurate *ab initio* parametrization of density functional dispersion correction (DFT-D) for the 94 elements H–Pu. *J. Chem. Phys.*, **132** (2010).

[34] Bardeen J., Shockley W. Deformation potentials and mobilities in non-polar crystals. *Phys. Rev.*, **80** (1950), 72-84.

[35] Tang X.M., Ou Q., Wang Z.Y. Positional isomerism of aromatic heterocyclic spacer cations in two-dimensional Dion-Jacobson hybrid perovskites. *J. Phys. Chem. Lett.*, **15** (2024), 9575-9584.

[36] Hellman A., Razaznejad B., Lundqvist B.I. Potential-energy surfaces for excited states in extended systems. *J. Chem. Phys.*, **120** (2004), 4593-4602.

[37] Jiang X., Xu Z., Zheng Y. Origin of broadband emission and large Stokes shift in antimony trisulfide. *J. Phys. Chem. Lett.*, **13** (2022), 8026-8032.

[38] Maurer R.J., Reuter K. Excited-state potential-energy surfaces of metal-adsorbed organic molecules from linear expansion Δ-self-consistent field density-functional theory (ΔSCF-DFT). *J. Chem. Phys.*, **139** (2013).

[39] Wei S.H., Zhang S.B. Chemical trends of defect formation and doping limit in II-VI semiconductors: the case of CdTe. *Phys. Rev. B*, **66** (2002), 155211.

[40] Zhang S.B., Wei S.H., Zunger A. Intrinsic *n*-type versus *p*-type doping asymmetry and the defect physics of ZnO. *Phys. Rev. B*, **63** (2001), 075205.

[41] Wang J., Uddin M.A., Chen B. Enhancing photostability of Sn-Pb perovskite solar cells by an alkylammonium pseudo-halogen additive. *Adv. Energy Mater.*, **13** (2023), 2204115.